

APPLIED SCIENCES AND ENGINEERING

Self-determined shapes and velocities of giant near-zero drag gas cavities

Ivan U. Vakarelski,^{1*} Evert Klaseboer,² Aditya Jetly,¹ Mohammad M. Mansoor,¹ Andres A. Aguirre-Pablo,¹ Derek Y. C. Chan,^{3,4*} Sigurdur T. Thoroddsen¹

Minimizing the retarding force on a solid moving in liquid is the canonical problem in the quest for energy saving by friction and drag reduction. For an ideal object that cannot sustain any shear stress on its surface, theory predicts that drag force will fall to zero as its speed becomes large. However, experimental verification of this prediction has been challenging. We report the construction of a class of self-determined streamlined structures with this free-slip surface, made up of a teardrop-shaped giant gas cavity that completely encloses a metal sphere. This stable gas cavity is formed around the sphere as it plunges at a sufficiently high speed into the liquid in a deep tank, provided that the sphere is either heated initially to above the Leidenfrost temperature of the liquid or rendered superhydrophobic in water at room temperature. These sphere-in-cavity structures have residual drag coefficients that are typically less than $1/10$ those of solid objects of the same dimensions, which indicates that they experienced very small drag forces. The self-determined shapes of the gas cavities are shown to be consistent with the Bernoulli equation of potential flow applied on the cavity surface. The cavity fall velocity is not arbitrary but is uniquely predicted by the sphere density and cavity volume, so larger cavities have higher characteristic velocities.

INTRODUCTION

One of the fundamental topics in fluid mechanics is the motion of a sphere in an ideal fluid that has zero viscosity and obeys the free-slip boundary condition where the tangential stress is zero on the sphere surface. Physically, this model only considers the effects of fluid inertia, and the analytical solution shows that the net force on the sphere is zero. This is because the pressure exerted by the fluid on the front half of the sphere exactly cancels that exerted on the rear hemisphere (1). For the same free-slip sphere moving in a Newtonian fluid with a constant viscosity, the effect of viscosity becomes small at high sphere velocities. This is quantified by a large Reynolds number, $Re \equiv \rho D_S U / \mu \gg 1$, which compares inertial forces to viscous forces, where ρ is the fluid density, D_S is the sphere diameter, U is the characteristic fluid velocity, and μ is the fluid dynamic viscosity. The drag force is expressed as $F_D \equiv C_D (\pi D_S^2 / 4) (\rho U^2 / 2)$, where, for a free-slip sphere, the drag coefficient has the limiting form $C_D \approx (48/Re)$ as $Re \rightarrow \infty$ (2–4) and thus decreases to zero as the speed increases. This is the well-known d'Alembert paradox (5). However, at a solid surface, the layer of fluid adjacent to it will move at the velocity of the solid, a condition referred to as the no-slip boundary condition that generates a boundary layer in which viscosity effects must be considered. This then provides the resolution to the d'Alembert paradox (5).

Although a sphere with a free-slip surface is a hypothetical model, it represents the theoretical limit at which hydrodynamic drag can be minimized. This notion provides the motivation to construct a surface that obeys the free-slip or zero tangential stress condition as far as possible and to investigate how this can be used to reduce drag and dissipation. The pursuit of this ideal limit can provide an important and fundamental contribution in the quest for energy-efficient transport.

However, it is challenging to experimentally produce a free-slip surface. Previous attempts to realize zero tangential stress surfaces for drag reduction include using bubble injection near the surface (6–8) and the use of superhydrophobic surfaces (9–12) or hot surfaces above the Leidenfrost temperature (13–15) to sustain a thin submillimeter gas layer that envelops a solid sphere. However, the limited thickness of the gas layers produced by these methods only resulted in a partial slip at the surface that can be characterized by a Navier slip length (16, 17). Supercavitation can be used to greatly reduce the drag on underwater projectiles, but this phenomenon takes place only at extremely high flow velocities, limiting its application to expensive supercavitating torpedo technologies (18, 19). In recent years, partial cavitation assisted by gas infusion has shown promising results in the quest for the development of energy-efficient, high-speed marine vehicles (6, 7).

Here, we demonstrate how a solid metal sphere falling in a liquid can be completely encased in a giant stable streamlined gas cavity that eliminates solid-liquid contact. These sphere-in-cavity structures were created by allowing a metal sphere of centimeter size to fall and have an impact on the free surface of a liquid held in a deep (2-m) tank. At a sufficiently high impact velocity, controlled by the release height above the liquid surface, the sphere entrains a cylinder of air while entering the liquid, which is then pinched off to form a streamlined teardrop-shaped gas cavity. The volume of the cavity was between 5 and 15 times that of the sphere as it travels down in the liquid. The cavity minimizes dissipation or drag by shedding small gas bubbles from the tail until it reaches the optimum size and shape and continues to travel at a constant velocity U , which is independent of the impact velocity of the sphere. This closed gas-liquid interface is a free-slip surface that cannot sustain a shear stress.

In a recent study (20), we investigated the detailed dynamics of the formation of stable streamlined gas cavities following the impact of a heated Leidenfrost sphere on a perfluorocarbon liquid, PP1 [perfluoro-2-methylpentane (C_6F_{14}); Flutec PP1, F2 Chemicals Ltd.]. An example of the steady fall of a Leidenfrost sphere-in-cavity structure that formed around a 10-mm steel sphere in this liquid is given in movie S1. Here, we demonstrate that this sphere-in-cavity can also be formed by dropping a metal sphere from air into a deep tank of water. In Fig. 1,

¹Division of Physical Science and Engineering, King Abdullah University of Science and Technology, Thuwal 23955-6900, Saudi Arabia. ²Institute of High Performance Computing, 1 Fusionopolis Way, Singapore 138632, Singapore. ³School of Mathematics and Statistics, University of Melbourne, Parkville, Victoria 3010, Australia. ⁴Department of Mathematics, Swinburne University of Technology, Hawthorn, Victoria 3122, Australia.

*Corresponding author. Email: ivanuriev.vakarelski@kaust.edu.sa (I.U.V.); d.chan@unimelb.edu.au (D.Y.C.C.)

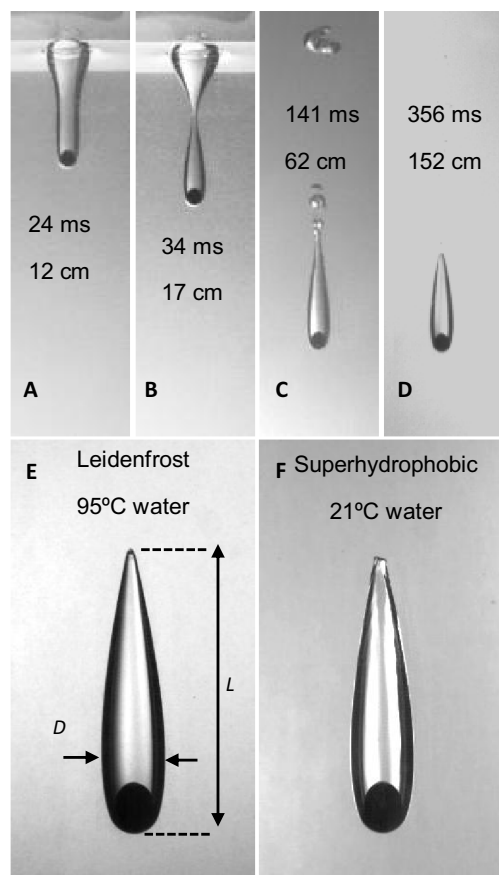


Fig. 1. Formation of a gas cavity around an impacting 20-mm-diameter steel sphere. Snapshots from movie S2 showing (A and B) the formation of a gas cavity around a hot 20-mm Leidenfrost steel sphere at sphere temperature $T_S = 400^\circ\text{C}$ as it enters a 2-m-tall tank containing water at 95°C and (C and D) the development and trajectory of the sphere-in-cavity structure at the indicated depths and times after entry. (E) A close-up of the steady-state gas cavity of length L and maximum diameter D formed around the 20-mm Leidenfrost steel sphere at $T_S = 400^\circ\text{C}$ in 95°C water. (F) The steady-state gas cavity formed around a cold 20-mm superhydrophobic steel sphere at $T_S = 21^\circ\text{C}$ in 21°C water.

we show examples of the formation of sphere-in-cavity structures due to the impact of a 20-mm-diameter steel sphere from air into a deep tank of water at 21° and 95°C . The entire process is shown in movie S2. Tungsten carbide spheres with density of about twice that of steel were also used. The sphere, located at the leading end or nose of the gas cavity, was separated from the gas-liquid interface by a thin gas layer. This gas layer can be sustained by the sphere when it is heated above the Leidenfrost temperature (21–23) before being dropped into the liquid (sphere temperature $T_S = 400^\circ\text{C}$ in 95°C water or $T_S = 230^\circ\text{C}$ in the fluorocarbon liquid PP1). In 21°C water, the gas layer at the sphere can be sustained by making the sphere surface superhydrophobic (24–26).

From analyzing high-speed video recordings of the path of these cavities, we can deduce that the magnitude of the drag coefficient, $C_D \approx 0.02$, is 10 times smaller than the magnitudes of the drag coefficients of solid teardrop-shaped plastic objects of the same dimensions made by three-dimensional (3D) printing. Therefore, we conclude that the gas cavity experiences near-zero drag. Because the Reynolds numbers of all cavity fall experiments range from 10^4 to 10^5 , the motion of the cavity can be described by the potential flow of an ideal fluid in an external

body force field, the gravitational field in this case. From this analysis, we can deduce the pressure inside the gas cavity. This physical model is reminiscent of the study of Davies and Taylor (27) of the rise velocity of a large spherical cap gas bubble in liquid.

We will first adduce experimental results to demonstrate that the sphere-in-cavity structure is nearly neutrally buoyant and has very small drag coefficients. In conjunction with the high Reynolds numbers, this justifies the use of potential flow theory to relate the observed shapes of the gas cavities to their velocity and show that they can be related by the application of the Bernoulli equation. The interior pressure of the cavity can be estimated from this modeling. Finally, we deduce that the velocity of the sphere-in-cavity structure that experiences near-zero hydrodynamic drag is not arbitrary. It is completely determined by the diameter of the solid sphere and the ratio of the sphere density to the liquid density. Because the volume of the gas cavity is found to be proportional to the density ratio, the velocity is then proportional to the cavity volume, or in other words, the larger cavities will travel at higher velocities.

RESULTS

Cavity shapes and volumes

The cavity size and fall velocity were determined using high-magnification videos. Examples of the fall of the sphere-in-cavities created by a 20-mm steel sphere are given in movie S3 for a Leidenfrost sphere in 95°C water (left video and Fig. 1E) and a superhydrophobic sphere in room temperature, 21°C water (right video and Fig. 1D). The self-determined teardrop-shaped gas cavities that minimized drag have self-similar shapes that depend on the combination of sphere material and liquid. The aspect ratio of cavity length L (~ 37 to 156 mm) to maximum diameter D (~ 11.5 to 31.8 mm) ranged from $L/D \sim 3.2$ for steel spheres in PP1 to $L/D \sim 5.6$ for tungsten carbide spheres in 95°C water (see table S1). See Fig. 1E for the definition of L and D .

The volume of the cavity was estimated by matching the video snapshots with a three-piece algebraic fitting curve (fig. S4). As shown in Fig. 2A, the ratio of the cavity volume V_C (V_C includes the volume of the sphere) to the volume of the metal sphere $V_S \equiv (\pi/6)D_S^3$, where D_S is the sphere diameter, is always just slightly smaller than the ratio of the sphere density to the fluid density ρ_S/ρ , ranging from 5 to 15. Therefore, the sphere-in-cavity structure is nearly neutrally buoyant. The volume of the gas cavity V_C is also observed to be related to the dimensions of the cavity by the relation $V_C \approx 0.46LD^2$ (Fig. 2B) for all combinations of sphere and fluid properties, which suggests that they have self-similar shapes.

We should note that the stability of the sphere-in-cavity formation is limited by the increase of hydrostatic pressure with depth during the fall. As can be seen in movie S2 for the 20-mm steel spheres, the formation is still stable upon reaching the bottom of the 2-m tank for both the Leidenfrost sphere in 95°C water and the superhydrophobic sphere in room temperature water. However, if the free fall continues long enough, the cavity will eventually collapse, as previously observed for smaller 10-mm Leidenfrost steel spheres falling in PP1 liquid (20). Here, we limit our consideration to the steady-state fall of sphere-in-cavity formation, assuming a constant ambient pressure over the length of the cavity in our theoretical analysis.

Sphere-in-cavity drag coefficients

We use the drag coefficient to quantify the near-zero hydrodynamic drag of the moving sphere-in-cavity. From the measured constant

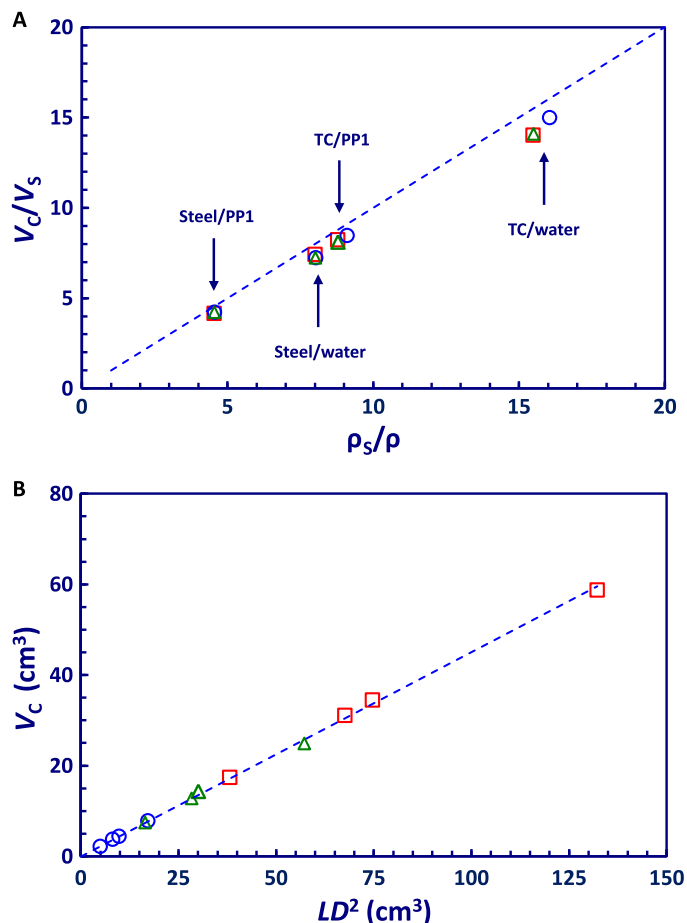


Fig. 2. Cavity volume variation. (A) Dependence of the cavity-to-sphere volume ratio V_C/V_S on the sphere-to-liquid density ratio ρ_S/ρ . Data are for 10-mm (blue circles), 15-mm (green triangles), and 20-mm (red squares) steel ($\rho_S = 7.7 \text{ g/cm}^3$) or tungsten carbide (TC) ($\rho_S = 14.9 \text{ g/cm}^3$) spheres falling in PP1 ($\rho = 1.7 \text{ g/cm}^3$) and 95°C water ($\rho = 0.96 \text{ g/cm}^3$). The dotted line corresponds to neutral buoyancy of the sphere-in-cavity structure. (B) Cavity volume, as a function of $(LD)^2$, cavity diameter D , and length L , for the same sphere sizes and liquid combination as in (A). The dotted line is the best linear fit to the data that gives the relation $V_C \approx 0.45 LD^2$.

free-fall velocity U of the cavity, we can deduce the drag coefficient C_D using the equation

$$C_D = \frac{8gM_{\text{eff}}}{\pi\rho D^2 U^2} \quad (1)$$

where g is the gravitational acceleration. The effective mass, $M_{\text{eff}} = m_S - \rho V_C$, of the sphere-in-cavity is found by obtaining the volume of the gas cavity V_C (which includes the sphere) from snapshots of the video frames (fig. S4) to calculate the buoyancy force that opposes the weight of the metal sphere m_S . In practice, because of the near cancellation of the weight and the buoyancy force, the value of M_{eff} is sensitive to the estimated cavity volume because the mean density of the sphere-in-cavity, (M_{eff}/V_C) , is found to be around 10 times smaller than the density of the surrounding fluid.

To demonstrate the near-zero drag coefficients of the streamlined cavity, we conducted complementary experiments using solid projectiles produced by 3D printing. The projectiles had the same streamlined

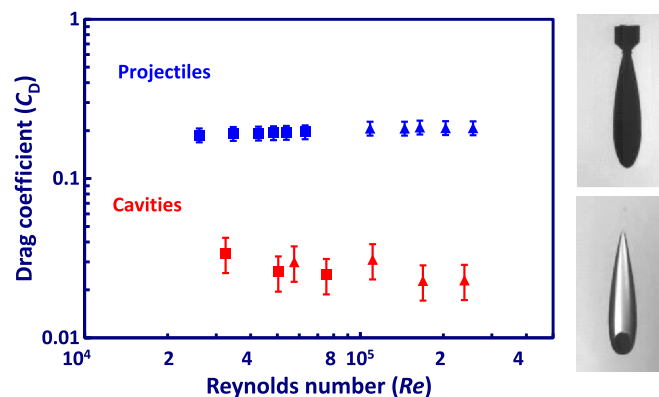


Fig. 3. Comparison of drag coefficients of cavities and solid projectiles of the same shape. Comparison of the variation of the drag coefficient C_D with Reynolds number Re for (i) lower data set: gas cavity in 21°C water around superhydrophobic steel spheres of diameter $D_S = 15, 20,$ and 25 mm (solid red squares) and around Leidenfrost steel spheres at $T_S = 400^\circ\text{C}$ in 95°C water of diameter $D_S = 10, 15, 20,$ and 25 mm (solid red triangles), and (ii) upper data set: the drag on solid replica projectiles: $D_P = 25 \text{ mm}$, $L_P/D_P = 4.5$ containing different weights in 21°C water (solid blue squares) and 95°C water (solid blue triangles). Side images are snapshots of the falling projectile and sphere-in-cavity from movie S4. Fins on the solid projectiles were added to ensure rectilinear free fall. Their effect on the magnitude of the drag coefficient is estimated to be less than 10%.

shape and dimensions (length L_P , maximum diameter D_P , and volume V_P) as the cavity (fig. S3) but were expected to have the usual “stick” boundary condition of any solid surface. The projectiles were hollow, so their mass m_P could be adjusted by inserting small metallic spheres (fig. S2). The drag on the projectile in free-fall experiments in the same liquid was estimated using the same relation (1) as for the cavity, but the effective mass $M_{\text{eff}} = m_P - \rho V_P$ can be adjusted over a wider range of projectile mean densities by changing m_P .

In Fig. 3, we show the variation of the drag coefficient C_D with the Reynolds number Re for steel sphere-in-cavities and similar replica solid projectiles falling in 21° or 95°C water. For the cavities, the variation of C_D with Re was obtained by changing the steel sphere diameter of 10 to 25 mm and water viscosity $\mu = 1.0 \text{ mPa}\cdot\text{s}$ at 21°C and $\mu = 0.3 \text{ mPa}\cdot\text{s}$ at 95°C. The variation of the projectile C_D with Re was obtained by changing the projectile weight while using the same projectile size $D_P = 25 \text{ mm}$ and with $L_P/D_P = 4.5$ matching the $L/D \approx 4.5$ ratio for the cavities formed around steel spheres. For Reynolds numbers in the range $Re \sim 2 \times 10^4$ to 3×10^5 , here, we estimated that the steel sphere-in-cavities have drag coefficients $C_D \approx 0.02$ to 0.03 or close to an order of magnitude lower than the solid projectile drag with coefficient $C_D = 0.20 \pm 0.02$. The marked difference in the hydrodynamic drag of the streamlined gas cavity around a 20-mm steel sphere and the corresponding solid projectile of approximately the same size, shape, and effective mass in free fall in 95° or 21°C water is best demonstrated in movie S4.

Another quantitative difference between the drag force experienced by gas cavities and solid projectiles can be observed in the variation of their drag coefficients C_D with the aspect ratio. For solid projectiles, the drag coefficients pass through a minimum at $L_P/D_P \sim 3$, reflecting the variation in the relative contributions to C_D from the skin and form drag with the aspect ratio. In the same regime of aspect ratios, the drag on the sphere-in-cavity seems to follow the opposite trend, decreasing with L/D between ~ 3.2 and 5.5 . This trend indicates that any increase in the skin drag component is negligible for the cavities (see fig. S6).

The residual drag of the sphere-in-cavity, however small, can still be associated with a large Navier slip length at the free surface. In a recent investigation, we used numerical simulation to quantify the relation between drag reduction and Navier slip length for the case of free-falling Leidenfrost spheres (16). In the future, similar numerical simulations of the present sphere-in-cavity configuration could be used to quantify the relationship between the residual drag and the giant Navier slip.

Potential flow model for cavity shape and velocity

Under our experimental conditions, the sphere-in-cavities are in the high-Reynolds number regime with the free-slip condition on the surface of the gas cavity. The inertial contribution to the hydrodynamic pressure in water is of the order $\frac{1}{2}\rho U^2 \sim 2000$ Pa, for a typical velocity $U \sim 2$ m/s. The magnitude of the gravitational pressure is $\rho gL \sim 1000$ Pa, with a cavity length $L \sim 100$ mm. These two pressures are comparable in magnitude and are both more than two orders of magnitude larger than the Laplace pressure $\sim \gamma/D$ because of the surface tension effects of water at $\gamma \sim 0.072$ N/m. These estimates suggest that potential flow theory in a gravitational field that provides the body force could adequately describe the physics of the falling cavities.

To verify this, we solved the Laplace equation $\nabla^2\phi = 0$ for the velocity potential, where ϕ from which the fluid velocity field $\mathbf{u} = \nabla\phi$ can be calculated. On the surface of the cavity, the pressure in the fluid is equal to the constant pressure P_C inside the cavity. Therefore, the application of Bernoulli equation on the surface of the cavity gives the relation

$$P = P_0 - \frac{1}{2}\rho u^2 - \rho g z = P_C \quad (2)$$

with position z measured from the tail of the cavity and P_0 being the reference pressure in the fluid, where $u = 0$ and $z = 0$.

Equation 2 implies that the variation of the square of the velocity u^2 on the cavity surface that is not close to the solid sphere is a linear function of z . To check the applicability of Eq. 2, we digitized images of a cavity to find its boundary and solved $\nabla^2\phi = 0$ for the velocity potential by the nonsingular boundary integral method (25) under the condition that the normal derivative $\partial\phi/\partial n$ or, equivalently, the normal component of the velocity at the interface is zero. The results for selected sphere-liquid combinations in various liquids are shown in Fig. 4. It is evident that along the body of the cavity, the variation of u^2 does obey the linear form given by Eq. 2.

Around the nose of the cavity, the interface must conform to a segment of the sphere of diameter $D_s = 2R_s$. The pressure variation around a sphere in potential flow is of the form (1)

$$P(r = R_s, \theta) - P_0 = \frac{1}{2}\rho U^2 \left[1 - \frac{9}{4} \sin^2\theta \right] \quad (3)$$

where θ is the angle relative to the z axis. It is clear from Fig. 4 that the pressure variation at the front of the cavity follows Eq. 3, with the pressure having the stagnation value $\frac{1}{2}\rho U^2$ at the front pole of the cavity. For a sphere, the minimum pressure occurs at the equator, $\theta = \pi/2$, and has a value of $(-\frac{5}{8}\rho U^2)$, whereas the minimum pressure at the cavity surface, from the simulations of the experiment, is around $(-0.2\rho U^2)$, which is less than one-third the magnitude of the minimum around a sphere.

At the tail of the cavity, $z = 0$, we see from Fig. 4 that $P \approx 0.1\rho U^2$ for all four cases. Thus, we see from Eq. 2 that this is the pressure P_C inside the gas cavity relative to P_0 .

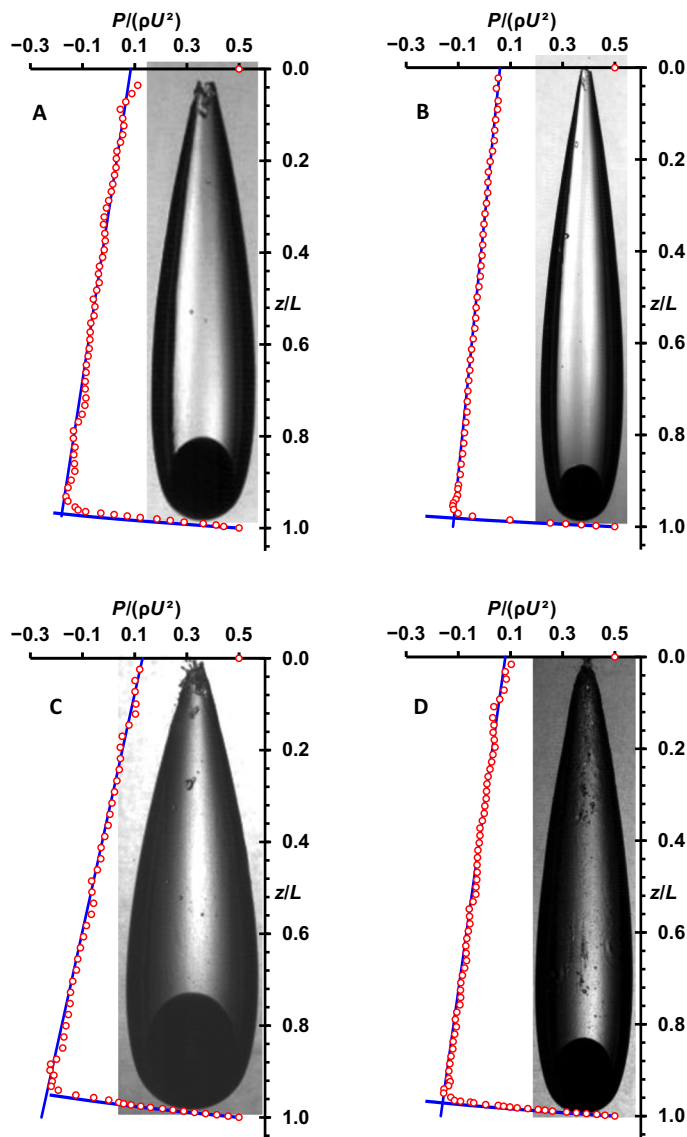


Fig. 4. Pressure variation on the cavity surface. Variation of the hydrodynamic pressure, $\rho u^2/2$ (symbols), obtained from potential flow and the gravitational, $\rho g z$ (solid line), components of the pressure on the surface of the gas cavity around 20-mm-diameter heated metal spheres in the Leidenfrost state (see Eq. 2) and the pressure around a sphere (dashed line) (see Eq. 3) for the systems: (A) steel sphere in 95°C water, (B) tungsten carbide sphere in 95°C water, (C) steel sphere in fluorocarbon PP1 liquid, and (D) tungsten carbide sphere in fluorocarbon PP1 liquid.

DISCUSSION

We have created a class of objects consisting of a giant gas cavity with a surface that surrounds a moving solid sphere but cannot sustain shear stresses. The cavity adopts a self-determined shape to minimize drag and dissipation. These sphere-in-cavity structures were formed by dropping Leidenfrost or superhydrophobic metallic spheres from air into a deep tank of liquid—hot and cold water as well as perfluorocarbon PP1 liquid. At an appropriate range of impact speeds, the column of air entrained by the sphere as it entered the liquid eventually pinched off and formed a teardrop-shaped gas cavity that completely enclosed the sphere and prevented contact between the solid and the liquid. As it falls in the liquid, this compound sphere-in-cavity structure adjusted its

shape and volume by shedding small bubbles from the tail to minimize dissipation and drag to attain a constant fall velocity corresponding to Reynolds number in the range $Re \sim 10^4$ to 10^5 and with a residual drag coefficient $C_D \approx 0.02$, which is only $1/10$ that of a streamlined solid projectile of the same dimensions. From the steady shape and volume of the cavity, we see that the geometry of the self-similar cavity and its steady velocity can be predicted by potential flow theory including gravity.

The physical mechanism of drag reduction by these giant gas cavities, which are 5 to 15 times the volume of the solid sphere, is fundamentally different from the existing drag reduction strategies, which are based on the creation of a submillimeter thin stable gas layer on solid surfaces to modify the hydrodynamic boundary condition from a no-slip to a partial slip. By using a large cavity, we essentially achieve the ideal case of a drag-free sphere-in-cavity structure.

However, the key observation is that although the sphere-in-cavity structure experiences near-zero hydrodynamic drag, its velocity U cannot be arbitrary because it must assume the value that generates a pressure profile that can balance the spatial variation of the gravitational potential. That is, the pressure variation must obey the Bernoulli equation (Eq. 2) on the cavity surface. The pressure variation at the nose of the cavity where its surface is separated from the solid sphere by a thin gas film follows the classic result of a free-slip sphere in potential flow from the stagnation value of $\frac{1}{2}\rho U^2$ at the front pole. The variation of the pressure on the cavity surface, as required by the Bernoulli equation in Fig. 4, only tracks this classical result for a sphere (dotted curve in Fig. 4) near the nose of the cavity. When the cavity surface is no longer close to the sphere, the pressure must assume a constant value, and the hydrodynamic pressure $\frac{1}{2}\rho U^2$ then transits sharply to the linear form in z as required by Eq. 2 to balance the gravitational pressure. The value of the internal pressure of the bubble can be found by extrapolating the linear part of the pressure curve to $z = 0$, giving an intercept value of $P_C \approx 0.1\rho U^2$ for the internal pressure of the cavity, relative to the reference value P_0 (see Fig. 4 and Eq. 2). At the tip of the cavity tail, the streamlines should converge in a cusp, but because of the large curvature around the tail, surface tension will break it up into an irregular shape. In the simulations, we extrapolated the cavity shape to a stagnation point at $z = 0$, where pressure must then again attain the stagnation value of $\frac{1}{2}\rho U^2$.

We now use a scaling argument to derive a simple relation between the velocity U and the properties of the sphere and the fluid. For a gas cavity of length L , the Bernoulli equation holds only over the portion $\sim [L - R_S]$ of the cavity surface that is not close to the solid sphere. Over this length, the pressure drop would balance the change in gravitational pressure, so we expect the scaling $\frac{1}{2}\rho U^2 \sim \rho g[L - R_S]$ or $U^2 \sim 2R_S[(L/R_S) - 1]$. We can now express the ratio (L/R_S) in terms of the density ratio between the sphere and the fluid, (ρ_S/ρ) , using two empirical results for the cavity volume V_C . From Fig. 2A, $V_C = V_S(\rho_S/\rho) = (\pi/6)D_S^3(\rho_S/\rho) \approx 0.5D_S^3(\rho_S/\rho)$; from Fig. 2B, $V_C = 0.46LD^2 \approx 0.5LD^2$; and on eliminating V_C , $(L/R_S) \approx 2(D_S/D)^2(\rho_S/\rho)$. Furthermore, from table S1 (A to C), we see that $(D_S/D)^2 \sim 2$. By combining these results, we can see in Fig. 5 that for a given sphere diameter D_S and a sphere-to-fluid density ratio ρ_S/ρ , the velocity of the sphere-in-cavity structure is quite accurately represented by the relation

$$U^2 \approx 3.3(gD_S)[(\rho_S/\rho) - 1] \approx 3.3(gD_S)[(V_C/V_S) - 1] \quad (4)$$

with the empirical value of the slope determined by a best-fit criterion. Because the cavity volume is also proportional to the density ratio, we conclude that the cavity velocity increases with cavity dimensions (Fig. 3), that

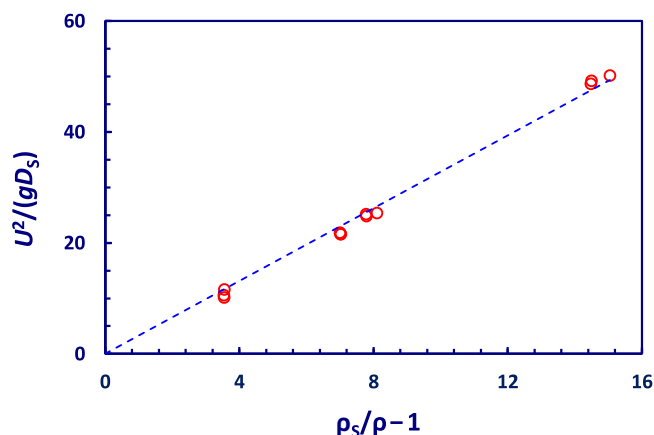


Fig. 5. Dependence of cavity velocity on sphere size and density ratio. Variation of the sphere-in-cavity velocity U with sphere diameter D_S and the sphere-to-fluid density ratio ρ_S/ρ . The dotted line is a linear best fit to the data that resulted in Eq. 4.

is, the larger is the cavity, the higher is its velocity. Equation 4 also ensures that the fall velocity $U = 0$ when $\rho_S = \rho$. The relation in Eq. 4 can thus be used to predict the velocity of any cavity generated by any nonwetting sphere free-falling in a liquid system.

We point out that the sphere-in-cavity shape is direction-dependent because the hydrostatic pressure gradient has a sign and a rising hollow sphere can never support this type of cavity shape. A sphere pulled rapidly upward would produce a cavity shape similar to a rising bubble (27). The cavity behind spheres moving rapidly in the horizontal direction will presumably generate more complicated asymmetric cavity shapes. One can envision spheres that can release or absorb gas from the cavity for speed control.

Finally, the shape and volume of the gas cavity and its velocity are constrained by the following factors. The radius of curvature of the nose of the cavity is determined by the radius of the solid sphere. From the movies presented in the Supplementary Materials, we see that during the transient stage of cavity formation, excess gas volumes are shed as bubbles at the tail of the cavity to attain a volume and shape as well as a fall velocity whereby the potential flow pressure distribution along its surface matches the linear gravitational pressure. Consequently, the a priori prediction of the optimal dimensions of a gas cavity and sphere size combination is a free boundary problem in potential flow theory in which the shape of the boundary is the solution to be sought. We defer this mathematical optimization problem to a future study.

MATERIALS AND METHODS

Spheres and liquids

The metal spheres are made of either steel (density, 7700 kg/m³; diameter, 10, 15, 20, and 25 mm) or tungsten carbide (density, 14,900 kg/m³; diameter, 10, 15, and 20 mm). The liquids are water at 21°C (density, 998 kg/m³; viscosity, 1 mPa·s), water at 95°C (density, 961 kg/m³; viscosity, 0.3 mPa·s), and the fluorocarbon PP1 (density, 1716 kg/m³; viscosity, 0.8 mPa·s), which is mostly composed of perfluoro-2-methylpentane (C₆F₁₄).

Experimental design and protocol

Experiments were conducted in a customized liquid tank with a height of 2 m and cross-sectional dimensions of 20 cm × 20 cm (fig. S1). An

electric heater was installed at the bottom of the tank that allowed the water in the tank to be heated up to 100°C.

A precondition for the formation of a stable streamlined cavity is that the impacting sphere should have a nonwetting surface. Thus, for experiments in 95°C water, the steel or tungsten carbide spheres were heated to about 400°C to produce a Leidenfrost state with nonwetting impact (14). For experiments in PP1, the spheres were heated to 230°C to produce a Leidenfrost state (20). In the case of the steel spheres in 21°C water, the nonwetting mode was achieved by modifying the sphere surface with a commercial superhydrophobic coating agent (Glaco Mirror Coat Zero, Soft99 Co.) (25).

Stable streamlined cavities only formed when the superhydrophobic or Leidenfrost sphere was released from a height ranging from 40 to 90 cm above the liquid surface, depending on the sphere size and density. However, we have not undertaken a detailed mapping of the sphere wake mode to the impact height as was done for the case of impact into PP1 liquid (20) but only adjusted the impact height for each type of sphere to ensure the creation of stable streamlined sphere-in-cavity formations. If the sphere-in-cavity can form, its final steady velocity does not depend on the initial impact velocity (20). Table S1 contains the release height used for each type of sphere to produce stable cavities.

Plastic projectiles used in the free-fall experiments to estimate the drag on solid surface streamlined bodies were produced using 3D printing. The projectiles are hollow so that their weight could be adjusted by inserting smaller metallic spheres to modify their mass. We designed a range of projectile shapes that matched the dimensions of the sphere streamlined cavity produced by the steel and tungsten carbide spheres. Figures S2 and S3 provide illustrations of these projectiles and the design details that match the cavity shape.

The fall of the sphere-in-cavity or of the plastic projectile in the liquid tank was recorded using a high-speed video camera (Photron FASTCAM SA5) with a typical filming frame rate of 2000 fps. The falling velocities were determined by image processing of the video clips (fig. S5). Higher-magnification snapshots of the sphere-in-cavities were used to estimate the cavity volume by piecewise fitting functions for each axisymmetric cavity shape. The nose of the cavity is represented by an arc of a circle of diameter D_s . A parabolic curve is used to fit the cavity shape between the tail and the widest part of the cavity with width D . An elliptical curve is used to join the parabolic tail portion to the spherical nose portion, which ensures continuity of the value and the slope of the three-piece fitting function (see fig. S4). A MATLAB image processing code was also used to digitize the cavity shape that is used as input to a fully desingularized axisymmetric boundary element method code (28) used to calculate the potential flow pressure profiles. This pressure calculation took less than 1 s to complete. Provided the images are clear and sharp, the two methods of extracting the cavity shape and estimating the cavity volume agree. Complete experimental details can be found in the Supplementary Materials.

SUPPLEMENTARY MATERIALS

Supplementary material for this article is available at <http://advances.sciencemag.org/cgi/content/full/3/9/e1701558/DC1>

section S1. Theory: Achieving near-zero drag at high Reynolds numbers

section S2. Stable streamlined cavity experiments

section S3. Solid projectile experiments

section S4. Determination of the drag coefficients

fig. S1. The experimental apparatus.

fig. S2. 3D-printed solid projectiles.

fig. S3. Comparison of shapes of sphere-in-cavities and solid projectiles.

fig. S4. Three-piece fitting function for the sphere-in-cavity.

fig. S5. Velocity versus depth data.

fig. S6. Dependence of the drag coefficient on the aspect ratio.

table S1A. Physical parameters of the sphere-in-cavities in 95°C water.

table S1B. Physical parameters of the sphere-in-cavities in 21°C water.

table S1C. Physical parameters of the sphere-in-cavities in PP1 liquid.

movie S1. Free fall of sphere-in-cavity for 10-mm Leidenfrost steel sphere in PP1.

movie S2. Impact and cavity formation by 20-mm steel sphere in 21° and 95°C water.

movie S3. Close-up of sphere-in-cavity for 20-mm steel sphere in 21° and 95°C water.

movie S4. Comparison of solid projectiles and sphere-in-cavity free fall.

Reference (29)

REFERENCES AND NOTES

- H. Lamb, *Hydrodynamics* (Dover Publications, 1932).
- V. G. Levich, Bubble motion at high Reynolds numbers. *Zh. Eksp. Teoret. Fiz.* **19**, 18–24 (1949).
- D. W. Moore, The boundary layer on a spherical gas bubble. *J. Fluid Mech.* **16**, 161–176 (1963).
- B. K. C. Chan, R. G. H. Prince, Distillation studies—Viscous drag on a gas bubble rising in a liquid. *AIChE J.* **11**, 176–192 (1965).
- G. K. Batchelor, *An Introduction to Fluid Dynamics* (Cambridge Univ. Press, 1967).
- S. L. Ceccio, Friction drag reduction of external flows with bubble and gas injection. *Annu. Rev. Fluid Mech.* **42**, 183–203 (2010).
- K. A. Lay, R. Yakushiji, S. A. Mäkiharju, M. Perlin, S. L. Ceccio, Partial cavity drag reduction at high Reynolds numbers. *J. Ship Res.* **54**, 109–119 (2010).
- R. A. Verschoof, R. C. A. van der Veen, C. Sun, D. Lohse, Bubble drag reduction requires large bubbles. *Phys. Rev. Lett.* **117**, 104502 (2016).
- J. P. Rothstein, Slip on superhydrophobic surfaces. *Annu. Rev. Fluid Mech.* **42**, 89–109 (2010).
- G. McHale, M. I. Newton, N. J. Shirtcliffe, Immersed superhydrophobic surfaces: Gas exchange, slip and drag reduction properties. *Soft Matter* **6**, 714–719 (2010).
- J. C. Brennan, N. R. Gerald, R. H. Morris, D. J. Fairhurst, G. McHale, M. I. Newton, Flexible conformable hydrophobized surfaces for turbulent flow drag reduction. *Sci. Rep.* **5**, 10267 (2015).
- S. Srinivasan, J. A. Kleingartner, J. B. Gilbert, R. E. Cohen, A. J. B. Milne, G. H. McKinley, Sustainable drag reduction in turbulent Taylor-Couette flows by depositing sprayable superhydrophobic surfaces. *Phys. Rev. Lett.* **114**, 014501 (2015).
- I. U. Vakarelski, J. O. Marston, D. Y. C. Chan, S. T. Thoroddsen, Drag reduction by Leidenfrost vapor layers. *Phys. Rev. Lett.* **106**, 214501 (2011).
- I. U. Vakarelski, D. Y. C. Chan, S. T. Thoroddsen, Leidenfrost vapour layer moderation of the drag crisis and trajectories of superhydrophobic and hydrophilic spheres falling in water. *Soft Matter* **10**, 5662–5668 (2014).
- D. Saranadhi, D. Chen, J. A. Kleingartner, S. Srinivasan, R. E. Cohen, G. H. McKinley, Sustained drag reduction in a turbulent flow using a low-temperature Leidenfrost surface. *Sci. Adv.* **2**, e1600686 (2016).
- I. U. Vakarelski, J. D. Berry, D. Y. C. Chan, S. T. Thoroddsen, Leidenfrost vapor layers reduce drag without the crisis in high viscosity liquids. *Phys. Rev. Lett.* **117**, 114503 (2016).
- A. Busse, N. D. Sandham, G. McHale, M. I. Newton, Change in drag, apparent slip and optimum air layer thickness for laminar flow over an idealised superhydrophobic surface. *J. Fluid Mech.* **727**, 488–508 (2013).
- E. Alyanak, R. Grandhi, R. Penmetsa, Optimum design of a supercavitating torpedo considering overall size, shape, and structural configuration. *Int. J. Solids Struct.* **43**, 642–657 (2006).
- D. Yang, Y. L. Xiong, X. F. Guo, Drag reduction of a rapid vehicle in supercavitating flow. *Int. J. Nav. Arch. Ocean* **9**, 35–44 (2017).
- M. M. Mansoor, I. U. Vakarelski, J. O. Marston, T. T. Truscott, S. T. Thoroddsen, Stable-streamlined and helical cavities following the impact of Leidenfrost spheres. *J. Fluid Mech.* **823**, 716–754 (2017).
- J. G. Leidenfrost, *De Aquae Communis Nonnullis Qualitatibus Tractatus* (Ovenius, 1756).
- J. O. Marston, I. U. Vakarelski, S. T. Thoroddsen, Cavity formation by the impact of Leidenfrost spheres. *J. Fluid Mech.* **699**, 465–488 (2012).
- D. Quéré, Leidenfrost dynamics. *Annu. Rev. Fluid Mech.* **45**, 197–215 (2013).
- C. Duez, C. Ybert, C. Clanet, L. Bocquet, Making a splash with water repellency. *Nat. Phys.* **3**, 180–183 (2007).
- I. U. Vakarelski, N. A. Patankar, J. O. Marston, D. Y. C. Chan, S. T. Thoroddsen, Stabilization of Leidenfrost vapour layer by textured superhydrophobic surfaces. *Nature* **489**, 274–277 (2012).
- M. M. Mansoor, J. O. Marston, I. U. Vakarelski, S. T. Thoroddsen, Water entry without surface seal: Extended cavity formation. *J. Fluid Mech.* **743**, 295–326 (2014).

27. R. M. Davies, G. I. Taylor, The mechanics of large bubbles rising through extended liquids and through liquids in tubes. *Proc. R. Soc. A* **200**, 375–390 (1950).
28. Q. Sun, E. Klaseboer, B. C. Khoo, D. Y. C. Chan, A robust and non-singular formulation of the boundary integral method for the potential problem. *Eng. Anal. Bound. Elem.* **43**, 117–123 (2014).
29. E. Achenbach, Experiments on the flow past spheres at high Reynolds numbers. *J. Fluid Mech.* **54**, 565–575 (1972).

Acknowledgments

Funding: This work was supported by the King Abdullah University of Science and Technology. D.Y.C.C. was supported by the Australian Research Council through Discovery Project grant no. DP170100376. **Author contributions:** I.U.V. conceived the research and designed the experiments. I.U.V., A.J., M.M.M., and A.A.A.-P. carried out the experiments. S.T.T. supervised the project, developed the image processing, and discussed the theoretical approach. E.K. and D.Y.C.C. undertook the theoretical interpretation and calculations.

D.Y.C.C. and I.U.V. wrote the manuscript with comments from all co-authors. **Competing interests:** The authors declare that they have no competing interests. **Data and materials availability:** All data needed to evaluate the conclusions in the paper are present in the paper and/or the Supplementary Materials. Additional data related to this paper may be requested from the authors.

Submitted 11 May 2017

Accepted 8 August 2017

Published 8 September 2017

10.1126/sciadv.1701558

Citation: I. U. Vakarelski, E. Klaseboer, A. Jetly, M. M. Mansoor, A. A. Aguirre-Pablo, D. Y. C. Chan, S. T. Thoroddsen, Self-determined shapes and velocities of giant near-zero drag gas cavities. *Sci. Adv.* **3**, e1701558 (2017).

Self-determined shapes and velocities of giant near-zero drag gas cavities

Ivan U. Vakarelski, Evert Klaseboer, Aditya Jetly, Mohammad M. Mansoor, Andres A. Aguirre-Pablo, Derek Y. C. Chan and Sigurdur T. Thoroddsen

Sci Adv 3 (9), e1701558.
DOI: 10.1126/sciadv.1701558

ARTICLE TOOLS

<http://advances.sciencemag.org/content/3/9/e1701558>

SUPPLEMENTARY MATERIALS

<http://advances.sciencemag.org/content/suppl/2017/09/01/3.9.e1701558.DC1>

REFERENCES

This article cites 26 articles, 2 of which you can access for free
<http://advances.sciencemag.org/content/3/9/e1701558#BIBL>

PERMISSIONS

<http://www.sciencemag.org/help/reprints-and-permissions>

Use of this article is subject to the [Terms of Service](#)

Science Advances (ISSN 2375-2548) is published by the American Association for the Advancement of Science, 1200 New York Avenue NW, Washington, DC 20005. 2017 © The Authors, some rights reserved; exclusive licensee American Association for the Advancement of Science. No claim to original U.S. Government Works. The title *Science Advances* is a registered trademark of AAAS.